PHYSICAL REVIEW B **91**, 085402 (2015)

Atomic structure of Bi_2Se_3 and Bi_2Te_3 (111) surfaces probed by photoelectron diffraction and holography

Mikhail V. Kuznetsov,[1] Lada V. Yashina,[2,*] Jaime Sánchez-Barriga,[3] Ilya I. Ogorodnikov,[1,4] Andrey S. Vorokh,[1]
Andrey A. Volykhov,[2,5] Roland J. Koch,[6] Vera S. Neudachina,[2] Marina E. Tamm,[2] Anna P. Sirotina,[2] Andrei Yu. Varykhalov,[3]
Gunther Springholz,[7] Günther Bauer,[7] John D. Riley,[8] and Oliver Rader[3]

[1]*Institute of Solid State Chemistry of the Ural Branch of the Russian Academy of Sciences, Pervomayskaya Street 91, 620990 Ekaterinburg, Russia*
[2]*Department of Chemistry, Moscow State University, Leninskie Gory 1/3, 119991 Moscow, Russia*
[3]*Helmholtz-Zentrum Berlin für Materialien und Energie, Elektronenspeicherring BESSY II, Albert-Einstein-Strasse 15, 12489 Berlin, Germany*
[4]*Ural Federal University, Mira Street 19, 620002 Ekaterinburg, Russia*
[5]*Institute of General and Inorganic Chemistry RAS, Leninsky Avenue 31, 119991 Moscow, Russia*
[6]*Institut für Physik, Technische Universität Chemnitz, Reichenhainer Strasse 70, 09126 Chemnitz, Germany*
[7]*Institut für Halbleiter und Festkörperphysik, Johannes Kepler Universität, Altenberger Strasse 69, 4040 Linz, Austria*
[8]*Department of Physics, La Trobe University, Bundoora, Victoria 3086, Australia*

(Received 8 September 2014; revised manuscript received 18 November 2014; published 2 February 2015)

Understanding how topologically protected surface states behave at surfaces and interfaces requires knowledge of the atomic structure. Whether the (111) surfaces of the prototypical topological insulators Bi_2Se_3 and Bi_2Te_3 are Bi or chalcogen terminated is the subject of current controversies. We employ photoelectron diffraction and holography, combining the advantages and avoiding the disadvantages of the contesting techniques previously used. We find bulklike chalcogen termination with a very small surface relaxation ($<1\%$) in agreement with density functional theory simulations. We prove the chalcogen termination for cleaved crystals and epitaxial films which shows the robustness of our conclusions.

DOI: 10.1103/PhysRevB.91.085402 PACS number(s): 68.35.B−, 71.20.Nr, 81.05.Hd

I. INTRODUCTION

Bismuth selenide and bismuth telluride present an iconic example of topological insulators (TIs). TIs are characterized by topologically protected states (TPSs) exhibiting a peculiar spin state where electron spins are locked perpendicular to their linear momenta. The TPS arises at the interface between a TI and a trivial insulator, for instance vacuum. The majority of previous studies on TIs, including the first observation of the TPS [1], are therefore related to the vacuum-surface interface.

Recent studies of Bi_2Se_3 by angle-resolved photoemission spectroscopy (ARPES) reveal strong changes of the topological surface state (TSS) dispersion upon modification of the surface by adsorption of residual gas [2,3], oxygen [4,5], NO [1], alkali metals [6], and 3*d* metals like Fe [7,8]. For these adsorption systems, the Dirac point has, however, been found to remain intact in agreement with the fact that the topological properties of the bulk dictate the topological protection. Surface chemistry and the resulting atomic configurations may, however, change the bulk band structure and possibly the topological properties in the near surface region. Strong surface reactivity of Bi_2Se_3 has been suggested separately for oxygen [9] and water [10] as a reason for surface degradation in air. Core-level photoemission studies in a very wide pressure range have resolved this problem, showing that the surface of the cleaved Bi_2Se_3 crystal is rather stable both in oxygen and in water vapor and a mixture of both as well, although the oxidation mechanism includes a simultaneous reaction with O_2 and H_2O [5].

Recently, a controversy evolved concerning the cleavage plane of Bi_2Se_3 single crystals, which have been used in most ARPES studies [1–7,9,10]. It is known that the bulk structure is composed of sheets of stacked X-Bi-X-Bi-X ($X =$ Se,Te) quintuple layers (QLs) followed by a van der Waals gap (see Fig. 1). The (111) surface of the crystal is the surface parallel to these QLs. A clean (111) surface is experimentally achieved by cleaving the crystal under vacuum. Similar to other layered compounds the natural cleavage plane is expected to be chalcogen terminated. However, the results of a recent low-energy ion scattering study contradict this expectation. Instead, low-energy ion scattering (LEIS), which is one of the few techniques giving a measure of the element composition at the very surface, results in Bi termination [11]. *I-V* low-energy electron-diffraction (LEED) and surface x-ray-diffraction (SXRD) data, however, turn out to be fully in agreement with the structural models derived from the bulk structure giving Se termination [12]. Similarly, for the Bi_2Te_3 (111) surface Te termination was reported [13].

In this work, we employ x-ray photoelectron diffraction (XPD), which combines the advantages of the previously used techniques to resolve these controversies. XPD is a powerful method which combines the element specificity of LEIS and the surface sensitivity of LEED, with the structural precision of LEED and SXRD, avoiding their disadvantages of possible surface damage in LEIS and of lack of element specificity and, hence, stronger model dependence of LEED. We cross-check the results by largely model-independent photoelectron holography (XPH). In XPH the diffraction pattern is considered as a hologram [14], which we convert into a real space image of the atomic structure.

---

[*] Yashina@inorg.chem.msu.ru

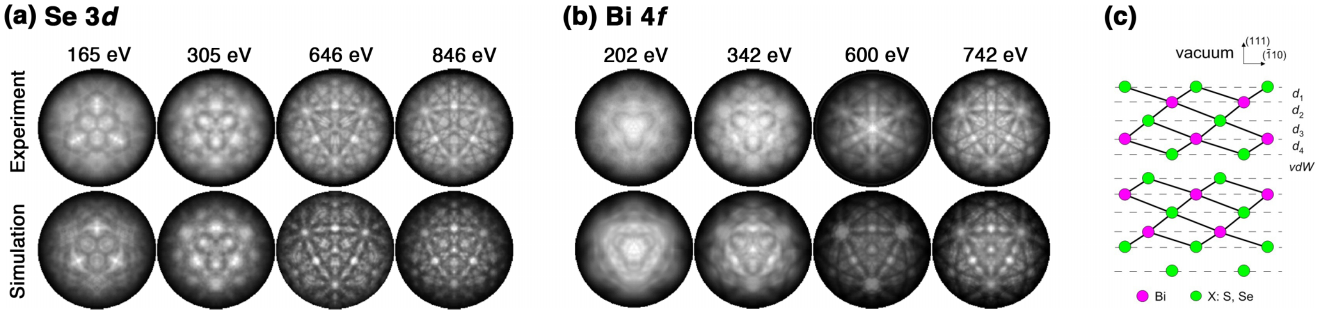

FIG. 1. (Color online) Experimental and EDAC simulated (for structure 1 with bulk parameters) XPD patterns obtained for the Bi_2Se_3 surface at different electron kinetic energies for the Se 3*d* (a) and Bi 4*f* (b) core levels. (c) Cross-sectional view of the Bi_2X_3 ($X =$ Se,Te) structure.

II. EXPERIMENTAL METHODS

Bismuth selenide and bismuth telluride *n*-type single crystals were grown using the Bridgman [15] method, whereas the thin films were produced using molecular-beam epitaxy (MBE) on BaF_2 (111) [16]. The bulk crystal structure parameters were determined by x-ray diffraction (XRD) and are in good agreement with the previously published results [17]. The single crystals were cleaved *in situ* under ultrahigh vacuum for the angle resolved photoelectron spectroscopy (ARPES), x-ray photoelectron spectroscopy (XPS), and x-ray photoelectron-diffraction (XPD) measurements. The high crystal quality of the obtained (111) surfaces was verified by low-energy electron diffraction (LEED) as well as the presence of the sharp features of the topological surface states and the valence band in the ARPES dispersions. The MBE films were decapped from a protective Se layer by a short annealing to 200 °C for 30 min inside the spectrometer shortly before the respective measurements were performed.

Photoemission experiments were carried out using several facilities of the Helmholtz-Zentrum Berlin, Germany. The ARPES experiments were performed in a ultrahigh vacuum chamber with a base pressure below 1×10^{-10} mbar using a Scienta R8000 electron analyzer at the UE112/PGM2a beamline using *p*-polarized undulator radiation. High-resolution XP spectra were recorded with high surface sensitivity (i.e., the kinetic energy of the photoelectrons was set between 50 and 100 eV) at the Russian-German beamline. The XPS spectra acquisition was performed using a SPECS Phoibos 150 electron energy analyzer at variable detection angles. The photoelectron-diffraction patterns were taken at the U49/PGM1 beamline using a toroidal electron energy analyzer [18].

To simulate our photoelectron-diffraction patterns for Bi_2X_3 the electron diffraction in atomic clusters (EDAC) software package [19] was used. The code is based on a multiple-scattering cluster approach, where the surface is represented by a sufficiently large number of atoms surrounding the emitter. We have performed simulations on parabolic clusters containing ∼1500–1900 bismuth and chalcogen atoms within a radius of 30 Å. For each emitter, which was placed in the center, we used an individual parabolic cluster. In all calculations we considered emitters belonging to the two topmost QLs.

Multiple elastic scattering of photoelectrons was modeled using a stable iterative technique until convergence was achieved. The calculations were performed for a temperature $T = 300$ K. Thermal vibrations were simulated using nonzero Debye temperatures for the bismuth and chalcogen atoms: $\theta_d^{\rm Bi}$, $\theta_d^{\rm Se}$, and $\theta_d^{\rm Te}$. By varying the radius of the parabolic clusters $R_{\rm max}$, the electronic surface position $z_{\rm surf}$, the Debye temperatures θ_d, the order of multiple scattering n, the inelastic mean free path, the number of emitters, as well as other parameters, the best agreement between experiment and simulation was obtained.

To obtain a quantitative value for the agreement between the calculated and the measured diffraction patterns an *R*-factor analysis was employed. We defined the *R* factor [20] as

$$R = \frac{\sum_n \left(\chi_n^{\rm th} - \chi_n^{\rm exp}\right)^2}{\sum_n \left[\left(\chi_n^{\rm th}\right)^2 + \left(\chi_n^{\rm exp}\right)^2\right]}, \tag{1}$$

where χ is the anisotropy of the angular intensity $\chi(\theta,\phi,k) = [I(\theta,\phi,k) - I_0(\theta,k)]/[I_0(\theta,k)]$ and $I_0(\theta)$ is an average value of the intensity for each polar angle $I_0(\theta,k) = 1/N \sum_i^N I(\theta,\phi,k)$.

X-ray photoelectron holography (XPH) was used to reconstruct three-dimensional (3D) images of the atomic structure around the emitter atom from the measured XPD patterns. The calculation was performed using the scattering pattern extraction algorithm with the maximum entropy method [21]. The reconstruction algorithm does not utilize the Fourier transformation, thus allowing us to obtain the atomic arrangement without the use of a multienergy format. To suppress image artifacts the algorithm uses the translational symmetry of the crystal in the lateral plane, namely, the unit-cell parameter as well as the real and reciprocal space filtration.

Theoretical modeling of the surface relaxation was performed within the density functional theory approach using the projected wave generalized gradient approximation method using the VIENNA *ab initio* simulation package (VASP) [22–24]. Core electrons were omitted by using the standard projector augmented wave pseudopotentials. In all simulations, a $(5 \times 5 \times 1)$ *k*-points mesh of the first Brillouin zone was used and no superlattice was employed. The parameters of the hexagonal lattice unit cell were fixed to their calculated bulk values, while the positions of all atoms were varied. We used slabs with one to five QLs; thicker slabs change the interatomic distances by less than 0.01 Å. Core-level shifts were calculated in the initial-state approximation as a variation of the electrostatic potentials at the atomic centers as described in Ref. [25].

III. RESULTS AND DISCUSSION

Using the unique opportunities provided by XPD and XPH in conjunction with x-ray photoelectron spectroscopy (XPS) and ARPES, we find no variation of the surface structure with time [11]. Our results demonstrate that both the surface termination and the layer sequence unequivocally correspond to the bulk ones with a very small surface relaxation, which is a contraction of about 1% of the first interlayer distance, and thus being within the accuracy of the methods employed.

A. XPD of Bi_2Se_3

The XPD patterns of the Bi 4*f* and Se 3*d* core levels for different kinetic energies between 100 and 850 eV are shown in Fig. 1 for the (111) surface of Bi_2Se_3. In this kinetic-energy region, multiple scattering events significantly contribute to the electron intensity distribution, as does forward scattering. By varying the kinetic energy, the probing depth can be varied. Furthermore the nature of the diffraction pattern changes: With increasing kinetic energy the contribution of forward scattering also increases [26].

Figure 1 also shows the simulated diffraction patterns presented here for comparison. We use the structural model of the surface as expected from the bulk structure, as shown in Fig. 1(c) (structure 1) and the bulk interlayer distances as indicated in Table I in Appendix B. This structural model, extracted directly from the bulk crystal structure, immediately gives a very good reproduction of the experimentally observed diffraction patterns. Similar results were obtained for Bi_2Te_3; the diffraction patterns are presented in Appendix A.

B. XPH of Bi_2Se_3

To discriminate between a chalcogen terminated surface and possible alternative structures, we applied photoelectron holography. Here, no assumptions about the structure are needed *a priori*. It therefore allows us to determine the layer sequence by first describing the local environment for each type of atoms. Using photoelectron holography, the 3D space surrounding a photoelectron emitter can be directly reconstructed from an XPD pattern. Previously, this relatively new method was successfully applied to visualize, with a moderate accuracy of ~ 0.5 Å, the atomic structure for simple cases of elemental solids, such as metals [27–29]. First successful applications of holography for compounds or alloys have also already been reported [30–32]. To reconstruct the atomic structure of TIs, we applied the scattering pattern extraction algorithm together with the maximum entropy method as described by Matsushita *et al.* [21,33].

Figure 2 shows a typical example of the local structure for a Se atom in the Bi_2Se_3 (111) surface layer using a hologram. The 3D real space image was calculated from the experimental diffraction pattern shown in Fig. 2(a). For a detailed analysis a cut along the gray plane in Fig. 2(a) is shown in Fig. 2(c) as a gray scale intensity image together with two line scans along A-A and B-B. In these profiles we observe overlaying atomic positions (marked with pink and green circles), hindering a straightforward interpretation. This complexity arises from different positions of the Se emitter atoms in the crystal lattice with respect to the surface, which

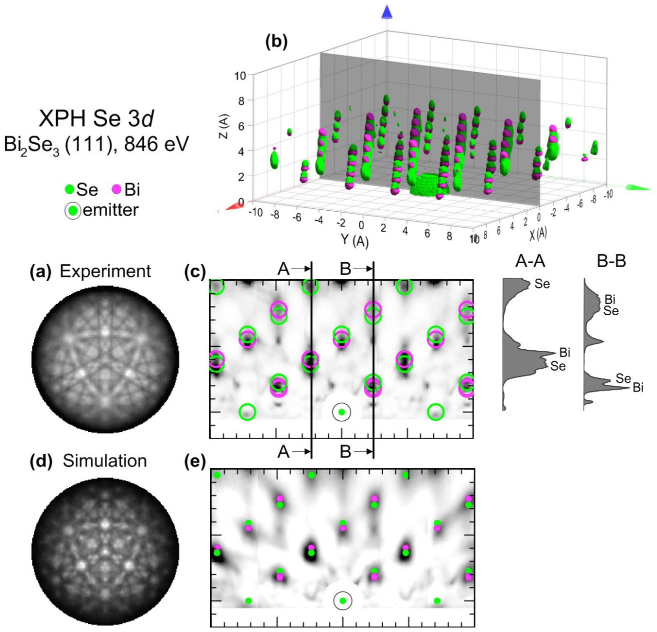

FIG. 2. (Color online) An example of the holographic reconstruction of a 3D-atomic structure for Se 3*d* obtained at a kinetic energy of 846 eV: an experimental XPD pattern (a); a real space image (b) and its cross section (c), a simulated XPD pattern (d), and a simulated real space image (e) obtained for the Se-terminated surface (structure 1).

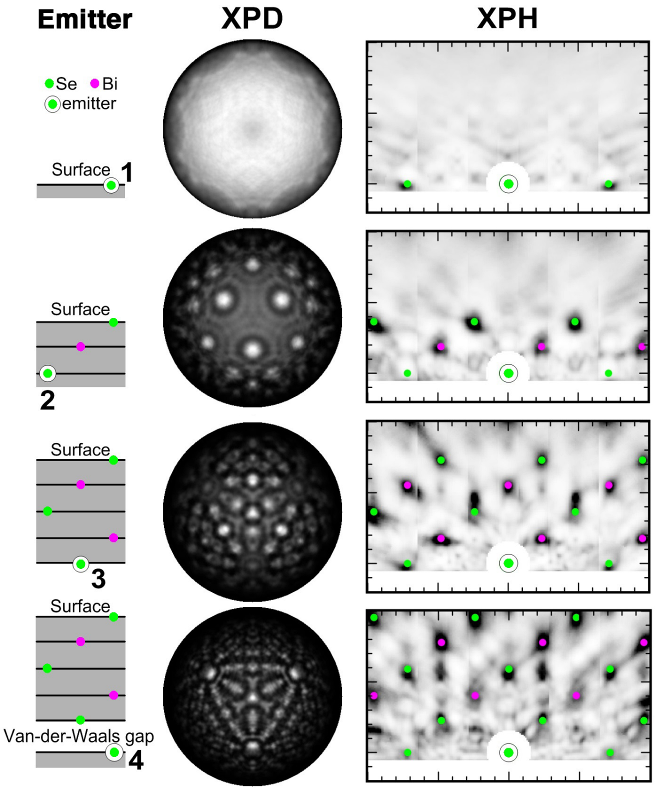

FIG. 3. (Color online) Contributions of different atomic positions of an Se emitter to the diffraction pattern and the real space image presented in Fig. 2(e): left column, emitter position (marked as atoms in ring); middle column, calculated XPD pattern for a given emitter; right column, calculated real space image for a given emitter.

are indistinguishable, at first sight, in the diffraction pattern. The result of their combination is illustrated in a simulation shown in Fig. 3: From row 1 to 4 we move the position of the emitter atom to a deeper atomic layer. The respective Se emitter atom is marked with a circle. Correspondingly we show the simulated diffraction pattern in the second column and finally in the third column we show the real space holography image calculated from the diffraction pattern.

The deeper in the bulk we place the emitter atom, the more complex the resulting holography image becomes. Simultaneously, the diffraction pattern comes closer to the one observed in the actual experiment (shown in Fig. 2). Using these simulated holography images we can now identify different contributions of the Se emitter atoms in the experimental holography image. The superposition of all contributions is presented in Fig. 2(d) in comparison with the experimental data and both images are in good agreement with each other.

The results of our calculations suggest that the bulk structure remains intact and that the surface is Se terminated after cleavage. All results are in good agreement with the Se-Bi-Se-Bi-Se layer sequence (structure 1). The same approach was applied for the Bi $4f$ holograms. Similar results were also obtained for the Bi_2Te_3 (111) surface, i.e., Te termination.

C. Surface termination

Furthermore, we investigated the sensitivity of these results to the surface termination. To examine the possibility of the Bi bilayer termination in more detail, we modeled both the corresponding core-level spectra using density functional theory and the photoelectron-diffraction patterns using the EDAC code for different structures presented in Fig. 4. Depending on the path for the surface loss of Se or enrichment in Bi, the following possible structures can be assumed: Bi-Bi-Se-Bi-Se-QLs (structure 2a), Bi-Bi-Se-QLs (structure 2b), and Bi-Bi-QLs (stucture 2c).

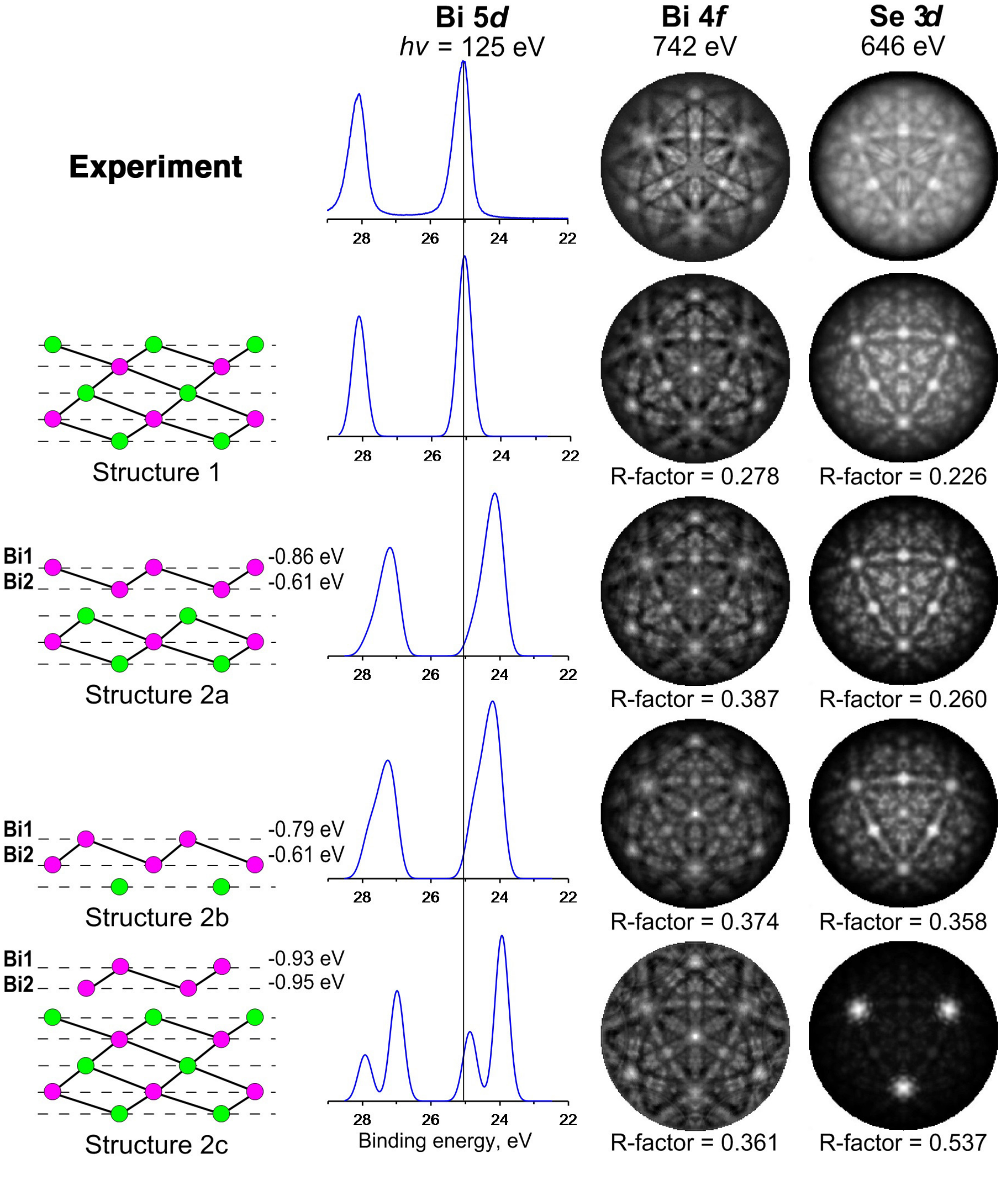

FIG. 4. (Color online) Different surface structures, the corresponding Bi $5d$ spectra, and Bi $4f$ and Se $3d$ diffraction patterns. R-factor values describing the correlation with experimental data are provided. The calculated chemical shifts are given for certain atomic layers relative to bulk.

The DFT simulation suggests that a bilayer Bi termination will result in a multicomponent character of the Bi 4*f* and Bi 5*d* spectra with a surface core-level shift in the range from −0.2 to −0.9 eV depending on the atomic position and structure. The detailed data are presented in Tables I and II and in Fig. 4, where theoretical XPS spectra are shown. As it follows from the comparison of the calculated spectra with the experimental ones, where Bi 5*d* is a single doublet, the concept of Bi termination is not consistent with our experimental observations. In addition, structures 2a, 2b, and 2c do not describe the experimental XPD pattern accurately, in contrast to the case of structure 1, as additionally demonstrated by the *R*-factor analysis.

D. Ion-beam damage

In order to simulate a possible beam damage caused by the LEIS experiment we sputtered the Bi_2Te_3 surface using 500-eV Ar^+ ions. Afterward a low-binding energy component as expected for Bi termination appears. Our results suggest that the Bi termination observed by the LEIS experiment [11] is rather caused by radiation damage from the ions than being exemplary for the undisturbed surface after cleavage. This damaging of the surface does not occur in our XPS, XPD, and XPH experiments, which also demonstrate the absence of a Bi bilayer at the surface as well as the intactness of the layer sequence once the surface is formed after cleavage.

E. Surface relaxation

Finally, we would like to address the question of the structural parameters with respect to a possible surface relaxation. The surface relaxation is untypical for any layered crystals since only weak van der Waals bonds are broken during the surface formation. The energy gained by relaxation of the surface is therefore expected to be rather small. Even in the case of ion-covalent compounds such as PbS and MgO, the surface relaxation, which decreases with the depth from the surface in an oscillatory manner, does not exceed a 3% contraction of the interatomic distance in the first layer [34]. Nevertheless, *I-V* LEED measurements [13] of the Bi_2Te_3 (111) surface from an as grown film show a 1% contraction of the first interatomic distance (d_1 in Fig. 1). In agreement with the LEED data, our DFT simulation actually shows a 1% relaxation relative to the bulk interlayer distance values for both Bi_2Te_3 and Bi_2Se_3 (111) surfaces, as summarized in Table I. However, such a small deviation from the bulk value is below the accuracy limit of our simulation. Conversely this means that if the relaxation does occur for these surfaces, it certainly does not exceed 1%.

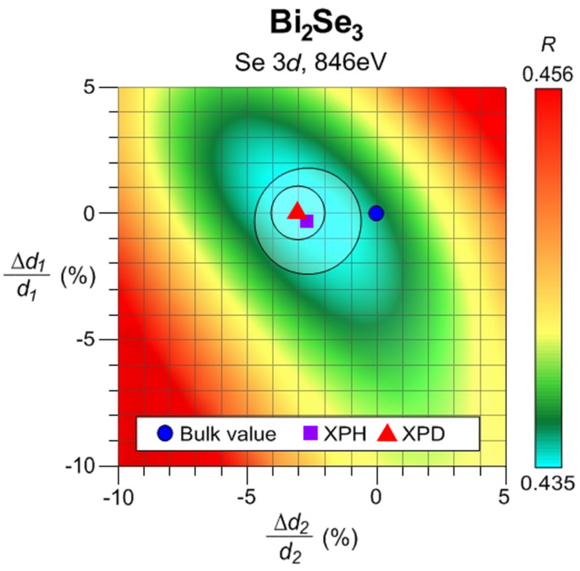

FIG. 5. (Color online) An example of the *R*-factor chart for the interatomic distances d_1 and d_2 optimization for the Se 3*d* diffraction pattern at an electron energy of 846 eV in the case of Bi_2Se_3.

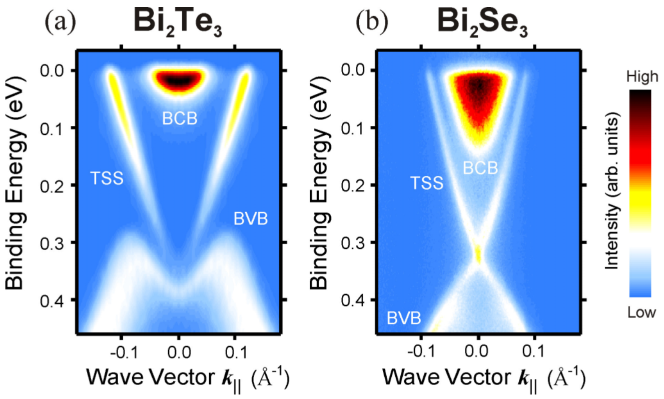

FIG. 6. (Color online) High resolution ARPES dispersions of the TSS, bulk conduction band (BCB) and bulk valence band (BVB) states of (a) Bi_2Te_3 and (b) Bi_2Se_3 obtained at photon energy of 21 eV and a temperature of 30 K.

To make sure that there are no artifacts resulting from the surface preparation, i.e., cleaving, we have measured the diffraction pattern for a clean Bi_2Se_3 (111) surface of a MBE grown film. Here, a clean surface was obtained by the *in situ* evaporation of a capping amorphous Se layer. The comparison of the data in Table I demonstrates fully identical results within the accuracy limits, despite the different sample preparation procedure.

Our data obtained from the *R*-factor analysis and within the XPH approach are in good agreement with the data obtained by LEED for both Bi_2Se_3 and Bi_2Te_3. The comparison of these data for Bi_2Se_3 is presented in Fig. 5 as an *R*-factor chart obtained as a function of two optimized structural parameters that describes the relaxation of the first ($\Delta d_1/d_{1\mathrm{bulk}}$) and second ($\Delta d_2/d_{2\mathrm{bulk}}$) interatomic distances. In this chart, the rings correspond to our confidence interval. Within this accuracy limit, the XPD, XPH, LEED, and DFT data are consistent with each other. Our results for Bi_2Te_3 are shown in Appendix A.

It is important to note that for all of our samples ARPES measurements (see Fig. 6) show the typical TSS states as expected [1]. These dispersions were stable over time, both at room and lower temperatures, thus linking our results directly to recent structural studies on TIs.

IV. CONCLUSION

To summarize, using a combined approach featuring x-ray photoelectron diffraction, holography, and spectroscopy combined, we demonstrated that the layer sequence at the (111) surfaces of Bi_2Se_3, Bi_2Te_3 bulk crystals, as well as Bi_2Se_3

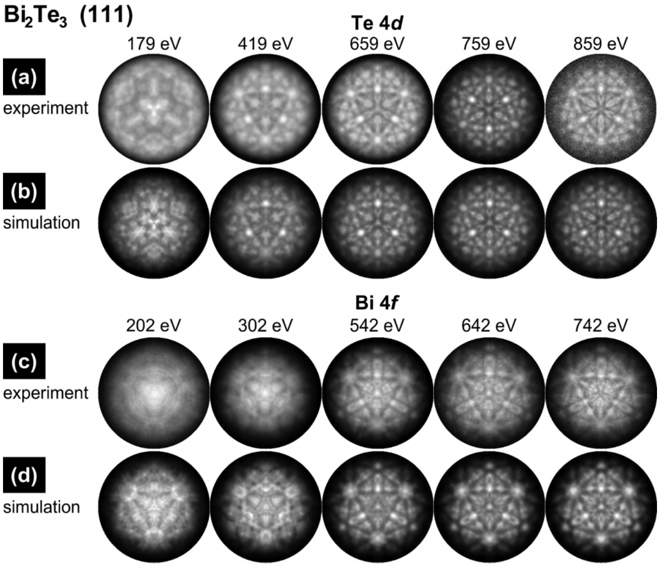

FIG. 7. Experimental (a,c) and EDAC simulated (structure 1 with bulk parameters [17]) (b,d) XPD patterns obtained for the Bi_2Se_3 surface at different electron kinetic energies for the Te 4*d* (a,b) and Bi 4*f* (c,d) core levels.

MBE-grown films correspond to the one of the bulk quintuple layer with a chalcogen termination. A small surface relaxation, especially a contraction of the first interatomic layer, cannot be excluded; however, the respective change in lattice constant does not exceed 1%.

ACKNOWLEDGMENTS

The authors acknowledge financial support within the bilateral program "Russian-German Laboratory at BESSY II" and thank the Helmholtz Zentrum (Berlin) for granting access to the beamlines UE112-PGM2a and U49-PGM1. The DFT (density functional theory) calculations were performed using SKIF and the "Lomonosov" supercomputer, Supercomputing Center of Lomonosov Moscow State University. The work was financially supported by DFG priority program SPP 1666, Impuls- und Vernetzungsfonds der Helmholtz-Gemeinschaft (Grant No. HRJRG-408) and Russian Foundation for Basic Research (Grant No. 13-02- 91327). A.P.S. acknowledges the support of the G-RISC (German-Russian Interdisciplinary Science Center) Centre of Excellence. M.V.K., I.I.O., and A.S.V. acknowledge the financial support of Russian Foundation for Basic Research (Grants No. 13-03-96032 and No. 14-02-31716) and Ural Branch of Russian Academy of Sciences (Grants No. 12-U-3-1006 and No. 12-M-23-2010). G.S. acknowledges the support of the Austrian Science Fund, Project SFB-025 IR-ON. The authors are grateful to Dr. Petar Stojanov and Dr. Anton Tadich for technical assistance and consultations.

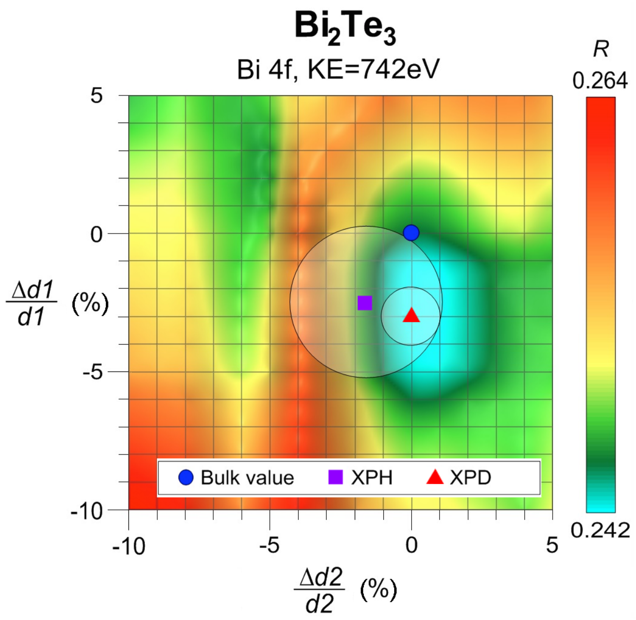

FIG. 8. (Color online) *R*-factor chart for the interatomic distances d_1 and d_2 optimization for the Bi 4*f* pattern obtained at 742 eV for Bi_2Te_3.

APPENDIX A: XPD OF Bi_2Te_3

In this Appendix we show the comparison of the experimental and simulated diffraction patterns for clean Bi_2Te_3 (111) surface obtained for Te 4*d* and Bi 4*f* core levels at different kinetic energies. They are presented in Fig. 7.

APPENDIX B: STRUCTURAL PARAMETERS

In this Appendix we summarize structural parameters for clean Bi_2Se_3 and Bi_2Te_3 (111) surfaces. The interlayer distances are listed in Tables I and II. The optimization of the structural parameters for Bi_2Te_3 is illustrated by R-factor chart at Fig. 8. Table III presents the calculated core level shifts for different structural models.

TABLE I. Summary of structural parameters of the (111) surface of Bi_2Se_3: In a QL, the Bi_2Se_3 $Se^1 - Bi^1 - Se^2 - Bi^2 - Se^3$ distances are $d_1 = Se^1 - Bi^1$, $d_2 = Bi^1 - Se^2$, $d_3 = Se^2 - Bi^2$, $d_4 = Bi^2 - Se^3$; vdW is the van der Waals gap distance.

	Bulk [3]	LEED [12] crystal	SXRD [12] crystal	XPD Se 3*d* crystal	XPH Bi 4*f* crystal	XPH Se 3*d* crystal	XPH Bi 4*f* film	DFT
d_1 (Å)	1.550	1.56 ± 0.03	1.51 ± 0.05	1.62 ± 0.02	1.60 ± 0.05	1.60 ± 0.05	1.60 ± 0.05	1.56
d_2 (Å)	1.931	1.96 ± 0.03	1.94 ± 0.06	1.91 ± 0.02	1.8 ± 0.1	1.90 ± 0.05	2.00 ± 0.05	1.96
d_3 (Å)	1.931	2.01 ± 0.04	1.91 ± 0.05	–	2.00 ± 0.05	2.00 ± 0.05	2.00 ± 0.05	1.94
d_4 (Å)	1.550	1.53 ± 0.05	1.72 ± 0.04	–	–	1.8 ± 0.1	1.70 ± 0.05	1.58
vdW (Å)	2.578	2.51 ± 0.08	2.50 ± 0.06	–	–	2.50 ± 0.05	2.20 ± 0.05	–

TABLE II. Summary of structural parameters of the (111) surface of Bi$_2$Te$_3$: In a QL, the Bi$_2$Te$_3$ Te^1 − Bi^1 − Te^2 − Bi^2 − Te^3 distances are d_1 = Te^1 − Bi^1, d_2 = Bi^1 − Te^2, d_3 = Te^2 − Bi^2, d_4 = Bi^2 − Te^3; vdW is the van der Waals gap distance.

	Bulk [3]	LEED [13] film	XPD Bi 4*f* crystal	XPD Te 4*d* crystal	XPH Bi 4*f* crystal	XPH Te 4*d* crystal	DFT
d_1 (Å)	1.743	1.68 ± 0.02	1.69 ± 0.02	1.71 ± 0.02	1.8 ± 0.1	1.70 ± 0.05	1.72
d_2 (Å)	2.033	2.03 ± 0.02	2.05 ± 0.02	2.03 ± 0.02	2.00 ± 0.05	2.00 ± 0.05	2.06
d_3 (Å)	2.033	2.02 ± 0.02	–	–	2.00 ± 0.05	2.00 ± 0.05	2.04
d_4 (Å)	1.743	1.71 ± 0.03	–	–	–	1.70 ± 0.05	1.74
vdW (Å)	2.612	2.57 ± 0.02	2.59 ± 0.02	2.59 ± 0.02	–	2.60 ± 0.05	–

TABLE III. Calculated Bi 5*d* core-level shifts (eV) for Bi-terminated Bi$_2$Se$_3$/Bi$_2$Te$_3$ (111) surfaces (the respective structures are shown in Fig. 4).

	Bi$_2$Se$_3$		Bi$_2$Te$_3$	
	Bi$_1$	Bi$_2$	Bi$_1$	Bi$_2$
Structure 2a	−0.89	−0.61	−0.94	−0.68
Structure 2b	−0.79	−0.51	−0.9	−0.64
Structure 2c	−0.93	−0.95	−1.12	−1.05

[1] M. Z. Hasan and C. Kane, Rev. Mod. Phys. **82**, 3045 (2010).

[2] M. Bianchi, S. Guan, J. Bao, B. Iversen, P. King, and P. Hofmann, Nat. Comm. **1**, 128 (2010).

[3] H. M. Benia, A. Yaresko, A. P. Schnyder, J. Henk, C. T. Lin, K. Kern, and C. R. Ast, Phys. Rev. B **88**, 081103 (2013).

[4] B. Zhou, Z. K. Liu, J. Analytis, K. Igarashi, S. Mo, D. Lu, R. Moore, I. Fisher, T. Sasagawa, Z. Shen, Z. Hussain, and Y. Chen, Semicond. Sci. Technol. **27**, 124002 (2012).

[5] L. Yashina, J. Sánchez-Barriga, M. R. Scholz, A. Volykhov, A. Sirotina, V. Neudachina, M. Tamm, A. Varykhalov, D. Marchenko, G. Springholz, G. Bauer, A. Knop-Gericke, and O. Rader, ACS Nano **7**, 5181 (2013).

[6] M. Bianchi, R. C. Hatch, Z. Li, P. Hofmann, F. Song, and J. Mi, ACS Nano **6**, 7009 (2012).

[7] M. R. Scholz, J. Sanchez-Barriga, D. Marchenko, A. Varykhalov, A. Volykhov, L. V. Yashina, and O. Rader, Phys. Rev. Lett. **108**, 256810 (2012).

[8] T. Valla, Z.-H. Pan, D. R. Gardner, Y. S. Lee, and S. Chu, Phys. Rev. Lett. **108**, 117601 (2012).

[9] D. S. Kong, J. J. Cha, K. J. Lai, H. L. Peng, J. G. Analytis, S. Meister, Y. L. Chen, H. J. Zhang, I. R. Fisher, and Z. X. Shen, ACS Nano **5**, 4698 (2011).

[10] H. M. Benia, C. Lin, K. Kern, and C. R. Ast, Phys. Rev. Lett. **107**, 177602 (2011).

[11] X. He, W. Zhou, Z. Y. Wang, Y. N. Zhang, J. Shi, R. Q. Wu, and J. A. Yarmoff, Phys. Rev. Lett. **110**, 156101 (2013).

[12] D. D. dos Reis, L. Barreto, M. Bianchi, G. A. S. Ribeiro, E. A. Soares, W. S. e Silva, V. E. de Carvalho, J. Rawle, M. Hoesch, C. Nicklin, W. P. Fernandes, J. Mi, B. B. Iversen, and P. Hofmann, Phys. Rev. B **88**, 041404(R) (2013).

[13] N. Fukui, T. Hirahara, T. Shirasawa, T. Takahashi, K. Kobayashi, and S. Hasegawa, Phys. Rev. B **85**, 115426 (2012).

[14] J. J. Barton, Phys. Rev. Lett. **61**, 1356 (1988).

[15] V. I. Shtanov and L. Yashina, J. Crystal Growth **311**, 3257 (2009).

[16] O. Caha, A. Dubroka, J. Humlicek, V. Holy, H. Steiner, M. Ul-Hassan, J. Sánchez-Barriga, O. Rader, T. Stanislavchuk, A. Sirenko, G. Bauer, and G. Springholz, Crystal Growth and Design **13**, 3365 (2013).

[17] S. Nakajima, J. Phys. Chem. Solids **24**, 479 (1963).

[18] G. Cousland, A. Smith, J. Riley, and A. Stampfl, J. Appl. Phys. **106**, 093510 (2009).

[19] F. J. Garcia de Abajo, M. A. Van Hove, and C. S. Fadley, Phys. Rev. B **63**, 075404 (2001).

[20] D. Woodruff and A. Gozalez-Elipe, Chem. Phys. Lett. **199**, 625 (1992).

[21] T. Matsushita, F. Matsui, H. Daimon, and K. Hayashi, J. Elecron. Spectrosc. Relat. Phenom. **178**, 195 (2010).

[22] G. Kresse and J. Hafner, Phys. Rev. B **47**, 558 (1993).

[23] G. Kresse and J. Hafner, Phys. Rev. B **48**, 13115 (1993).

[24] G. Kresse and J. Hafner, Phys. Rev. B **49**, 14251 (1994).

[25] L. Yashina, T. Zyubina, R. Püttner, A. Zyubin, V. I. Shtanov, and E. Tikhonov, J. Phys. Chem. C **112**, 19995 (2008).

[26] M. Kuznetsov, I. Ogorodnikov, and A. Vorokh, Russ. Chem. Rev. **83**, 13 (2014).

[27] S. Hardcastle, Z.-L. Han, G. Harp, J. Zhang, B. Chen, D. K. Saldin, and B. Tonner, Surface Science **245**, L190 (1991).

[28] T. Greber, J. Phys.: Cond. Mat. **13**, 10561 (2001).

[29] C. Fadley, M. Van Hove, A. Kaduwela, S. Omori, L. Zhao, and S. Marchesini, J. Phys.: Cond. Mat. **13**, 10517 (2001).

[30] F. Matsui, N. Nishikayama, H. Matsui, K. Goto, M. Hashimoto, T. Hatayama, T. Matsushita, Y. Kato, S. Tanaka, and H. Daimon, J. Phys. Soc. Jpn. **80**, 013601 (2011).

[31] A. Uesaka, K. Hayashi, T. Matsushita, and S. Arai, Phys. Rev. Lett. **107**, 045502 (2011).

[32] K. Kataoka, F. Matsui, Y. Kato, T. Matsushita, K. Hattori, and H. Daimon, Surf. Rev. Lett. **13**, 209 (2006).

[33] T. Matsushita, F. Z. Guo, M. Suzuki, F. Matsui, H. Daimon, and K. Hayashi, Phys. Rev. B **78**, 144111 (2008).

[34] N. V. Skorodumova, K. Hermansson, and B. Johansson, Phys. Rev. B **72**, 125414 (2005).